An examination of the homentropic Euler equations with averaged characteristics ☆

Gregory J. Norgard[1], Kamran Mohseni [*,2]

University of Colorado, Boulder, CO 80309-0429, USA

A B S T R A C T

This paper examines the properties of the homentropic Euler equations when the characteristics of the equations have been spatially averaged. The new equations are referred to as the characteristically averaged homentropic Euler (CAHE) equations. An existence and uniqueness proof for the modified equations is given. The speed of shocks for the CAHE equations are determined. The Riemann problem is examined and a general form of the solutions is presented. Finally, numerically simulations on the homentropic Euler and CAHE equations are conducted and the behaviors of the two sets of equations are compared.

© 2009 Elsevier Inc. All rights reserved.

1. Introduction

This manuscript examines a modification of the homentropic Euler equations where the characteristics of the equations have been spatially averaged. The equations examined are

$$\rho_t + \bar{u}\rho_x + \rho\frac{\bar{a}}{a}u_x = 0, \tag{1a}$$

$$u_t + \bar{u}u_x + \frac{a\bar{a}}{\rho}\rho_x = 0, \tag{1b}$$

$$\bar{u} = g * u, \tag{1c}$$

$$\bar{a} = g * a \tag{1d}$$

with $a^2 = \gamma\rho^{\gamma-1}$. These are derived in Section 2. The inspiration for these equations came from previous work done on a similarly modified Burgers equation.

The Burgers equation, $u_t + uu_x = 0$, is considered a simplistic model of compressible flow. Multiple independent investigations have been made into a modified Burgers equation with an averaged convective velocity [1–6],

$$u_t + \bar{u}u_x = 0, \tag{2a}$$

$$\bar{u} = g^\alpha * u, \tag{2b}$$

$$g^\alpha = \frac{1}{\alpha}g\left(\frac{x}{\alpha}\right) \tag{2c}$$

where g is an averaging kernel. A brief summary of the primary results are as follows.

1. Solutions to Eqs. (2) exist and are unique [2,4].
2. When the initial conditions are C^1, the solution remains C^1 for all time [4].
3. For bell shaped initial conditions it was proven that as the averaging approaches zero ($\alpha \to 0$), the solutions to Eq. (2) converge to the entropy solution of inviscid Burgers equation [5].
4. There is a set of discontinuous initial conditions where solutions to Eq. (2) will converge to a non-entropic solution, but these solutions are unstable [3,5].
5. It is conjectured that solutions to Eq. (2) will converge to the entropy solution of inviscid Burgers equation for all continuous initial conditions, and thus the scheme

$$u_t + \bar{u}u_x = 0, \tag{3}$$

$$\bar{u} = g^\alpha * u, \tag{4}$$

$$u(x, 0) = g^\alpha * u_0(x) \tag{5}$$

will converge to the entropy solution for any bounded initial condition u_0 [5].

The work on the regularization of the Burgers equation is inspired by and related to work done on the LANS-α equations [7–13]. These equations also employ an averaged velocity in the nonlinear term and have been successful in modeling some turbulent incompressible flows.

It is thought that a similar regularization could be accomplished for the equations that describe compressible flow. Encouraged by the results for Burgers equation, the next step is to attempt to introduce averaging into the one-dimensional homentropic Euler equations, a simplified version of the full Euler equations, where pressure is purely a function of density. There have been several attempts at such a regularization.

Using a Lagrangian averaging technique Bhat and Fetecau [14] derived the following equations

$$\rho_t + (\rho u)_x = 0, \tag{6}$$

$$w_t + (uw)_x - \frac{1}{2}\left(u^2 + \alpha^2 u_x^2\right)_x = -\frac{p_x}{\rho}, \tag{7}$$

$$\rho w = \rho v - \alpha^2 \rho_x u_x, \tag{8}$$

$$v = u - \alpha^2 u_{xx}. \tag{9}$$

While the solutions to the system remained smooth and contained much structure it was found that the equations were "not well-suited for the approximation of shock solutions of the compressible Euler equations."

Another attempt by Bhat, Fetecau, and Goodman used a Leray-type averaging [15] leading to the equations

$$\rho_t + \bar{u}\rho_x + \rho u_x = 0, \tag{10}$$

$$u_t + \bar{u}u_x + \frac{p_x}{\rho} = 0, \tag{11}$$

$$u = \bar{u} - \alpha^2 \bar{u}_{xx} \tag{12}$$

with $p = \kappa \rho^\gamma$. They then showed that weakly nonlinear geometrical optics (WNGO) asymptotic theory predicts the equations will have global smooth solutions for $\gamma = 1$ and form shocks in finite time for $\gamma \neq 1$.

Additionally in 2005, H.S. Bhat et al. [16] applied the Lagrangian averaging approach to the full compressible Euler equations. Their approach was successful in that a set of Lagrangian Averaged Euler (LAE-α) equations were derived. However, the equations seemed so intractable that they seemed impractical for real world applications.

Inspired by the existence uniqueness proofs from the averaged Burgers equations found in [2, 4], we average the characteristics of the homentropic Euler equations to derive what we term as the characteristically averaged homentropic Euler (CAHE) equations (1). It is the properties of these equations that this paper examines.

The following section follows the derivation and present the final equations. The existence and uniqueness of solutions to the equations are then proven in Section 3. Sections 4 and 5 examine the speed of the shocks and solutions to the Riemann problem. Numerical simulations and their comparison to those of the homentropic Euler equations are discussed in Sections 6 and 7. The results are then briefly summarized in the concluding remarks.

2. Derivation of the equations

2.1. The homentropic Euler equations

We begin the process of deriving the CAHE equations by starting with the homentropic Euler equations. There are two equations to the homentropic Euler equations. Conservation of mass and conservation of momentum. Pressure is expressed purely density raised to the power of γ,

$$\rho_t + (\rho u)_x = 0, \tag{13a}$$

$$(\rho u)_t + \left(\rho u u + \rho^\gamma\right)_x = 0. \tag{13b}$$

The equations are then written in primitive variable form

$$\begin{bmatrix} \rho \\ u \end{bmatrix}_t + \begin{bmatrix} u & \rho \\ \frac{a^2}{\rho} & u \end{bmatrix} \begin{bmatrix} \rho \\ u \end{bmatrix}_x = 0 \tag{14}$$

with $a^2 = \gamma \rho^{\gamma-1}$.

G.J. Norgard, K. Mohseni / J. Differential Equations ••• (••••) •••–•••

To get a clear view of the characteristics involved the equations are then diagonalized to obtain the equations

$$
\begin{bmatrix} v^+ \\ v^- \end{bmatrix}_t + \begin{bmatrix} u+a & 0 \\ 0 & u-a \end{bmatrix} \begin{bmatrix} v^+ \\ v^- \end{bmatrix}_x = 0 \tag{15}
$$

where

$$
v^+ = u + \frac{2a}{\gamma - 1}, \tag{16a}
$$

$$
v^- = u - \frac{2a}{\gamma - 1}. \tag{16b}
$$

The variables $v^\pm$ are commonly known as Riemann invariants. From Eq. (15) it is easy to see that the quantity v^+ is convected at speed $u+a$ and v^- speed $u-a$. Thus along the characteristics $u \pm a$, $v^\pm$ will remain constant.

Shocks will form when characteristics intersect. To prevent this from happening the characteristics are spatially averaged. This averaging is conducted by convoluting the variable to be averaged with an averaging kernel, g, and is represented by a bar above the variable. For example, the averaged velocity would be expressed

$$
\bar{u} = g * u. \tag{17}
$$

2.2. The averaging kernel

Several assumptions on the averaging kernel are made at this point. The kernel is assumed to be even, for isotropic purposes. For the purpose of Theorems 3.1 and 3.2 the kernel and its first derivative are assumed to be integrable. Of special interest is the Helmholtz filter which is defined as

$$
u = \bar{u} - \bar{u}_{xx}, \tag{18}
$$

and thus has an averaging kernel of

$$
g(x) = \frac{1}{2} \exp(-|x|). \tag{19}
$$

For all numerical simulations found in Sections 5, 6, and 7 the Helmholtz filter is used for its convenient inversion techniques.

Furthermore the kernel will be equipped with a parameter α which will control the amount of averaging. If g is the averaging kernel, then α is introduced as

$$
g^\alpha = \frac{1}{\alpha} g\left(\frac{x}{\alpha}\right). \tag{20}
$$

Thus as $\alpha \to 0$ the averaging kernel approaches the Dirac delta function.

2.3. Obtaining the CAHE equations

Using the averaging kernel discussed above the characteristics of the homentropic Euler equations are averaged to obtain the CAHE equations in diagonalized form,

$$
\begin{bmatrix} v^+ \\ v^- \end{bmatrix}_t + \begin{bmatrix} \bar{u}+\bar{a} & 0 \\ 0 & \bar{u}-\bar{a} \end{bmatrix} \begin{bmatrix} v^+ \\ v^- \end{bmatrix}_x = 0. \tag{21}
$$

Change the equations back into the primitive variable form and we get the equations

$$\rho_t + \bar{u}\rho_x + \rho\frac{\bar{a}}{a}u_x = 0,$$

$$u_t + \bar{u}u_x + \frac{a\bar{a}}{\rho}\rho_x = 0,$$

$$\bar{u} = g * u,$$

$$\bar{a} = g * a$$

with $a^2 = \gamma\rho^{\gamma-1}$ which were seen earlier as Eqs. (1).

These are now the equations that will be examined for the rest of this paper and are referred to as the characteristically averaged homentropic Euler (CAHE) equations. We begin by proving that Eqs. (1) have one and only one solution.

3. Existence and uniqueness theorem

A critically important property for Eqs. (1) to have is that a solution exists. This section addresses this problem by presenting a proof for the existence and uniqueness of solutions. This proof uses a method of characteristics approach and is similar to the existence uniqueness proof of Convectively Filtered Burgers equation found in [4].

An outline of the proof is as follows. When the equations are cast into their characteristic form, it is clear to see that the fluid velocity and the speed of sound remain bounded. Since those speeds remain bounded, the first derivative of the averaged speeds will remain bounded as well. The characteristics are governed by the averaged speeds and with the first derivatives bounded, the characteristics may grow closer, but will never intersect. Thus the solution can be fully realized by the characteristics and the initial conditions.

Theorem 3.1. *Let $g(\mathbf{x}) \in W^{1,1}(\mathbb{R})$ and $u_0(x), a_0(x) \in C^1(\mathbb{R})$, then there exists a unique global solution $u(x,t), a(x,t) \in C^1(\mathbb{R}, \mathbb{R})$ to Eqs. (1) with initial conditions*

$$u(x, 0) = u_0, \tag{22a}$$

$$a(x, 0) = a_0 \tag{22b}$$

with $a^2 = \gamma\rho^{\gamma-1}$.

Proof. Express Eqs. (1a) and (1b) with matrices as

$$\begin{bmatrix} \rho \\ u \end{bmatrix}_t + \begin{bmatrix} \bar{u} & \rho\frac{\bar{a}}{a} \\ \frac{a\bar{a}}{\rho} & \bar{u} \end{bmatrix} \begin{bmatrix} \rho \\ u \end{bmatrix}_x = 0. \tag{23}$$

By diagonalizing the matrix these equations can be rewritten as

$$\begin{bmatrix} v^+ \\ v^- \end{bmatrix}_t + \begin{bmatrix} \bar{u} + \bar{a} & 0 \\ 0 & \bar{u} - \bar{a} \end{bmatrix} \begin{bmatrix} v^+ \\ v^- \end{bmatrix}_x = 0. \tag{24}$$

It is here that we shift our perspective to a method of characteristics type view. Associate the maps $\phi^\pm$ with the characteristics of $v^\pm$. Thus we have

$$\frac{\partial}{\partial t}\phi^+(\xi,t) = \bar{u}\big(\phi^+(\xi,t),t\big) + \bar{a}\big(\phi^+(\xi,t),t\big), \tag{25}$$

$$\frac{\partial}{\partial t}v^+ = 0 \quad \text{along a } \phi^+ \text{ characteristic} \tag{26}$$

and

$$\frac{\partial}{\partial t}\phi^-(\xi,t) = \bar{u}\big(\phi^-(\xi,t),t\big) - \bar{a}\big(\phi^-(\xi,t),t\big), \tag{27}$$

$$\frac{\partial}{\partial t}v^- = 0 \quad \text{along a } \phi^- \text{ characteristic.} \tag{28}$$

From this we can obtain the estimates that

$$\big\|v^\pm(x,t)\big\|_{L^\infty} = \big\|v^\pm(x,0)\big\|_{L^\infty}. \tag{29}$$

If the mappings $\phi^\pm$ have continuously differentiable inverses, $\varphi^\pm$, then Eq. (24) has the solution

$$v^\pm(x,t) = v_0^\pm\big(\varphi^\pm(x,t)\big). \tag{30}$$

Sufficient conditions for such inverses to uniquely exist is if the Jacobians of $\phi^\pm$ are non-zero for all positions and time. Thus if $J(\phi^\pm) \neq 0$, Eq. (24) is uniquely solved by (30).

For the next section of the proof we will be dealing with ϕ^+. The results for ϕ^- follow in precisely the same manner. Since we are dealing with 1D the Jacobian of ϕ^+ is essentially ϕ_x^+. It is clear from Eq. (25) to see that the time derivative of ϕ_x^+ is

$$\frac{\partial}{\partial t}\phi_x^+ = (\bar{u}_x + \bar{a}_x)\phi_x^+. \tag{31}$$

Thus we see that

$$\phi_x^+ = \phi_x^+(0)\exp\left(\int_0^t \bar{u}_x + \bar{a}_x \, dt\right). \tag{32}$$

Thus ϕ_x^+ will remain non-zero if $|\int_0^t \bar{u}_x + \bar{a}_x \, dt| < \infty$.

First we will show that $u, a \in L^\infty$. We see that

$$\|2u\|_{L^\infty} = \left\|\frac{2a}{\gamma-1} + u + u - \frac{2a}{\gamma-1}\right\|_{L^\infty}$$

$$\leqslant \|v^+\|_{L^\infty} + \|v^-\|_{L^\infty}. \tag{33}$$

Looking at Eq. (29) and noting that $\|v^+\|_{L^\infty}$ and $\|v^-\|_{L^\infty}$ are bounded for all time, then $\|u\|_{L^\infty}$ is bounded for all time. Similarly one can bound the quantity $\|a\|_{L^\infty}$ for all time.

Given that $g(x) \in W^{1,1}(\mathbb{R})$, there exists $M \in \mathbb{R}$, such that

$$\left\|\frac{\partial}{\partial x}g\right\|_{L^1} \leqslant M < \infty. \tag{34}$$

Knowing that $\frac{\partial}{\partial x} g \in L^1$ and $u \in L^\infty$, we know that $\frac{\partial}{\partial x} \bar{u}$ exists and that

$$\frac{\partial}{\partial x} \bar{u} = \frac{\partial}{\partial x} g * u.$$

Similarly

$$\frac{\partial}{\partial x} \bar{a} = \frac{\partial}{\partial x} g * a.$$

Using Young's inequality we can bound the derivatives $\bar{u}_x$ and $\bar{a}_x$. We get

$$\left\| \frac{\partial}{\partial x} \bar{u} \right\|_{L^\infty} \leqslant \left\| \frac{\partial}{\partial x} g \right\|_{L^1} \|u\|_{L^\infty} \leqslant M \|u\|_{L^\infty}, \tag{35}$$

$$\left\| \frac{\partial}{\partial x} \bar{a} \right\|_{L^\infty} \leqslant \left\| \frac{\partial}{\partial x} g \right\|_{L^1} \|a\|_{L^\infty} \leqslant M \|a\|_{L^\infty}. \tag{36}$$

This leads directly to the bound

$$\left| \int\limits_0^t \bar{u}_x + \bar{a}_x \, dt \right| < M \big(\|u\|_{L^\infty} + \|a\|_{L^\infty} \big) t. \tag{37}$$

Thus for finite time, the Jacobian of $\phi^\pm$ remains uniquely invertible, with a continuously differentiable inverse and thus (30) is a unique $C^1(\mathbb{R})$ solution to (24). A unique $C^1(\mathbb{R})$ solution to Eqs. (1) follows accordingly. $\quad\square$

Theorem 3.2. *Let $g(\mathbf{x}) \in W^{1,1}(\mathbb{R})$ and $u_0(x), a_0(x) \in L^\infty(\mathbb{R})$, then there exists a unique global solution $u(x,t), a(x,t) \in L^\infty(\mathbb{R}, \mathbb{R})$ to Eqs. (1) with the initial conditions*

$$u(x, 0) = u_0, \tag{38a}$$

$$a(x, 0) = a_0. \tag{38b}$$

Proof. The proof is the same as for Theorem 3.1. $\phi^\pm$ still have unique continuously differentiable inverses, and the solution remains in the same form as Eq. (30), but now lacks continuity due to the initial conditions. $\quad\square$

It should be noted that different averagings can be used for $\bar{u}$ and $\bar{a}$. The existence and uniqueness proof will hold as long as a bound on the first derivatives of $\bar{u}$ and $\bar{a}$ remains constant. This is noted as the type of averaging used will affect shock speed as noted in Section 4.

4. Shock speeds

One of the consequences of the previous sections is that for continuous initial conditions, the solution will remain continuous. Also for initial conditions with a discontinuity, that discontinuity will remain. There are no colliding characteristics. Thus the "shock" is really a discontinuity that is being convected. If there is a discontinuity in $v_0^+(x)$ then that discontinuity will travel at speed $\bar{u}(x^*) + \bar{a}(x^*)$, where x^* is the location of the discontinuity. Similarly, if there is a discontinuity in $v_0^-(x)$ then that discontinuity will travel at speed $\bar{u}(x^*) - \bar{a}(x^*)$.

Consider the case where there is a single jump discontinuity in v^+, but otherwise constant:

$$v^+(x) = \begin{cases} v_l^+, & x < 0, \\ v_r^+, & x \geqslant 0, \end{cases} \tag{39a}$$

$$v^-(x) = C. \tag{39b}$$

This will lead to a jump discontinuity in u and in a.

With $\bar{u}$ and $\bar{a}$ defined as in Eqs. (1) and the filter g being even and $\int g = 1$ then the speed of the discontinuity in Eqs. (39) will be

$$s = \frac{u_l + u_r}{2} + \frac{a_l + a_r}{2} \tag{40}$$

where u_l, u_r, a_l and a_r are the limiting values of u and a on the left and right side of the discontinuity respectively.

Similarly, if the jump discontinuity existed only in v^- then the speed of the discontinuity would be

$$s = \frac{u_l + u_r}{2} - \frac{a_l + a_r}{2}. \tag{41}$$

For multiple discontinuities or for nonconstant values around the discontinuities, the values of $\bar{u}$ and $\bar{a}$ cannot generally be analytically written. However, for small values of α the filter will not "see" as far and the values of $\bar{u}$ and $\bar{a}$ will be roughly the average of the values just to the left and right of the discontinuity.

4.1. Alternative averagings and shock speeds

In the above calculation $\bar{u}$ and $\bar{a}$ were defined using the definition

$$(\bar{\cdot}) = g * (\cdot). \tag{42}$$

This is not, however, the only way to conduct averaging. One possible alternative is using Favre averaging, a density weighted average, where

$$(\bar{\cdot}) = \frac{g * (\rho \, \cdot)}{g * (\rho)}. \tag{43}$$

This alternative will not affect the existence uniqueness theorems established in Section 3. It will, however, change the shock speeds established earlier.

If Eq. (43) is used, the speed of a discontinuity in v^+ will travel at

$$s = \frac{\rho_l u_l + \rho_r u_r}{\rho_l + \rho_r} + \frac{\rho_l a_l + \rho_r a_r}{\rho_l + \rho_r}. \tag{44}$$

Another possibility is to apply a spatial average to the conserved quantities, density and momentum, and then compute the characteristic speeds from the averaged conserved quantities,

$$\tilde{u} = \frac{\overline{\rho u}}{\bar{\rho}}, \tag{45}$$

$$\tilde{a}^2 = \gamma (\bar{\rho})^{\gamma - 1}. \tag{46}$$

If the speeds of the characteristics were defined using $\tilde{u}$ and $\tilde{a}$, then the speed of the shocks would be

$$s = \frac{\rho_l u_l + \rho_r u_r}{\rho_l + \rho_r} + \sqrt{\gamma}\left(\frac{\rho_l + \rho_r}{2}\right)^{\frac{\gamma - 1}{2}}. \tag{47}$$

Thus how one chooses to define $\bar{u}$ and $\bar{a}$ will affect the speed of the discontinuities.

5. Riemann solutions

This section builds upon the results of Section 4 and establishes properties of the solutions of the CAHE equations for the Riemann problem. It then continues on to examine solutions of the CAHE equations if, instead of the Riemann problem, the initial conditions are slightly perturbed.

5.1. Riemann problem

Looking at Eq. (30), it is clear that any discontinuity that exists in the initial condition remains in the solutions for all time. Furthermore, no additional discontinuities will form.

For the Riemann problem, at time $t = 0$ a single discontinuity will exist at the origin:

$$u(x, 0) = \begin{cases} u_l, & x < 0, \\ u_r, & x \geqslant 0, \end{cases} \tag{48}$$

$$a(x, 0) = \begin{cases} a_l, & x < 0, \\ a_r, & x \geqslant 0, \end{cases} \tag{49}$$

which can also be rewritten in terms of the variables v^+ and v^-:

$$v^+(x, 0) = \begin{cases} v_l^+, & x < 0, \\ v_r^+, & x \geqslant 0, \end{cases} \tag{50}$$

$$v^-(x, 0) = \begin{cases} v_l^-, & x < 0, \\ v_r^-, & x \geqslant 0. \end{cases} \tag{51}$$

These discontinuities will travel at the speeds discussed in Section 4. We denoted the locations of the discontinuities in v^+ and v^- as x^- and x^+. The speeds of these discontinuities are determined by

$$\frac{\partial}{\partial t} x^{\pm} = \bar{u}(x^{\pm}) \pm \bar{a}(x^{\pm}). \tag{52}$$

Clearly the discontinuity found in v^+ will travel at a faster speed than the discontinuity in v^-. Thus the solution will consist of three different areas separated by the locations of x^- and x^+. The solution is then

$$v^+(x, t) = \begin{cases} v_l^+, & x < x^+(t), \\ v_r^+, & x^+(t) \leqslant x, \end{cases} \tag{53}$$

$$v^-(x, t) = \begin{cases} v_l^-, & x < x^-(t), \\ v_r^-, & x^-(t) \leqslant x. \end{cases} \tag{54}$$

If expressed in primitive variables the solution is

$$u(x,0) = \begin{cases} u_l, & x < x^-(t), \\ u_m, & x^-(t) \leqslant x < x^+(t), \\ u_r, & x^+(t) \leqslant x, \end{cases} \tag{55a}$$

$$a(x,0) = \begin{cases} a_l, & x < x^-(t), \\ a_m, & x^-(t) \leqslant x < x^+(t), \\ a_r, & x^+(t) \leqslant x, \end{cases} \tag{55b}$$

where $u_m = \frac{v_l^+ + v_r^-}{2}$ and $a_m = \frac{\gamma - 1}{2} \frac{v_l^+ - v_r^-}{2}$.

Thus in general, the Riemann problem will produce the solutions presented in Eqs. (55) where two discontinuities will propagate dependent upon the speeds of the averaged velocity and speed of sound. If the initial conditions happen to be chosen, such that v^+ or v^- are constant, then there will exist only one traveling discontinuity. The following subsection shows numerical simulations of a typical Riemann solution.

5.1.1. Riemann solution numerics

In Section 6, a numerical scheme is described that numerically simulates the behavior of the CAHE equations. However in Section 5.2 it is demonstrated that some of the solutions to the Riemann problem are unstable and thus cannot be captured by the numerical scheme. Thus this numerical scheme was developed. Since the Riemann problem solutions are of the form presented in Eqs. (55), finding solutions, even unstable ones, to the Riemann problem reduces to tracking the locations of the discontinuities in time. The following numerical scheme does precisely this.

To find the solution (55), the values $u_{l,m,r}$ and $a_{l,m,r}$ are all known, one simply has to determine the location of $x^{\pm}$. This is done by using Eq. (52). A typical iteration is as follows.

1. The values of $u(x, t_1)$ and $a(x, t_1)$ are known on a uniform grid.
2. The Helmholtz operator is then numerically inverted to give the values of $\bar{u}$ and $\bar{a}$ on the uniform grid. These values are then interpolated to give the values of $\bar{u} \pm \bar{a}$ at $x^{\pm}$.
3. The positions of the $x^{\pm}$ are then advanced in time by the values of $\bar{u} \pm \bar{a}$ on $x^{\pm}$ calculated in the previous step.
4. The values of $u(x, t_2)$ and $a(x, t_2)$ are now known using Eq. (55) and current positions of $x^{\pm}$.

The inversion of the Helmholtz operator is described in Section 6.

To examine a typical case, we will simulate the Riemann solution with the initial conditions

$$u(x,0) = \begin{cases} 0, & x < 0, \\ 0, & x \geqslant 0, \end{cases} \tag{56a}$$

$$a(x,0) = \begin{cases} 2, & x < 0, \\ 1, & x \geqslant 0. \end{cases} \tag{56b}$$

This set of initial conditions will be referred to as Example 1a. This is a standard shock tube problem where the velocity is zero initially and there is a jump in pressure. The initial conditions can be seen in Fig. 1. With these values there are discontinuities in variables v^+ and v^-. These discontinuities are seen to propagate to the right and left respectively as seen in Fig. 2. These numerical simulations were conducted with 2^{10} grid points on the domain $[-1, 1]$ with $\alpha = 0.02$.

5.2. The perturbed Riemann problem

While the solution to the Riemann problem generally leads to one or two traveling discontinuities, we have found that some of these traveling discontinuities are unstable.

There have been examinations of the Burgers equation with the characteristics averaged [1–5]. In two of these papers it was seen that certain traveling discontinuities in these equations were unstable
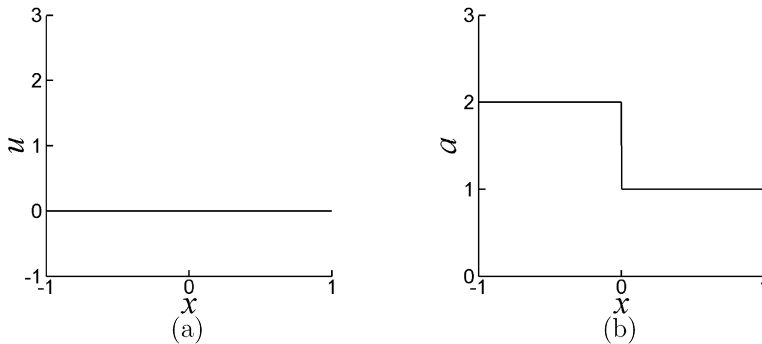
Fig. 1. The initial conditions for the Riemann problem. (a) The initial velocity profile is $u = 0$. (b) The initial speed of sound profile is a simple jump discontinuity, indicating a higher pressure on the left.
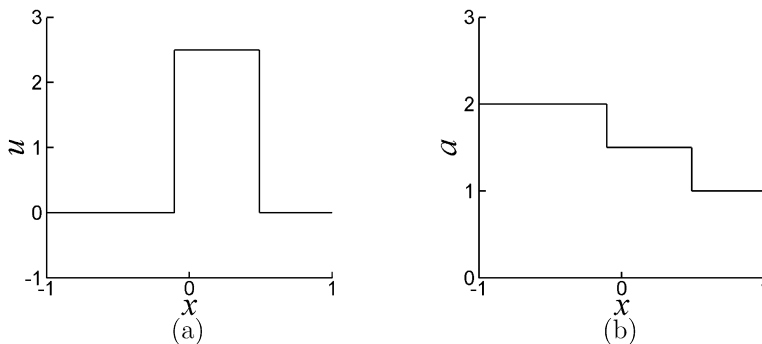

Fig. 2. The solution to the Riemann problem with initial conditions Eq. (56). There are two shocks found in both the velocity and speed of sound. This is the solution at time $t = 0.2$.

and if perturbed would become expansion waves [3,5]. We have found similar behavior for the CAHE equations.

Consider Example 1a as seen in Fig. 2. The position of the leftmost shock is denoted x^-. The value of $u - a$ is greater to the right of x^- than it is to the left. So clearly $\bar{u} - \bar{a}$ is increasing across the discontinuity at x^-. Thus the v^- characteristics are diverging there. This is typically indicative of an expansion wave. However, the spreading of this discontinuity remains simply a discontinuity.

Suppose instead that instead of a strict discontinuity, the function was a continuous function, albeit extremely steep. The diverging characteristics would then spread this extremely steep gradient and gradually make it less steep, forming an expansion wave. Thus, this traveling discontinuity is unstable, and any amount of smoothing would lead to an expansion wave as opposed to a shock.

Using numerics discussed in Section 6, we made runs using the same initial conditions as in Example 1a except the initial conditions were initially "smoothed," using the same Helmholtz filter as employed in the averaging of the characteristics. We will refer to this as Example 1b. This smoothing of the initial conditions is similar to the approach used in [5]. Fig. 3 shows the initial conditions where the smoothing is readily apparent in the a variable. Fig. 4 shows the solution at time $t = 0.2$. The right shock remains unchanged from the unperturbed solution seen in Fig. 2. However, an expansion wave is clearly seen on the left in the perturbed solution where previously there was a discontinuity. These simulations were run with a resolution of 2^{10} grid points and $\alpha = 0.02$.

To summarize, the solutions to the Riemann problem take the form of Eqs. (55) and produces one or two traveling discontinuities, some of which may be unstable. If instead the discontinuities in the initial conditions are replaced with steep, but continuous gradients, then the results will begin to include expansion waves in addition to the shocks.
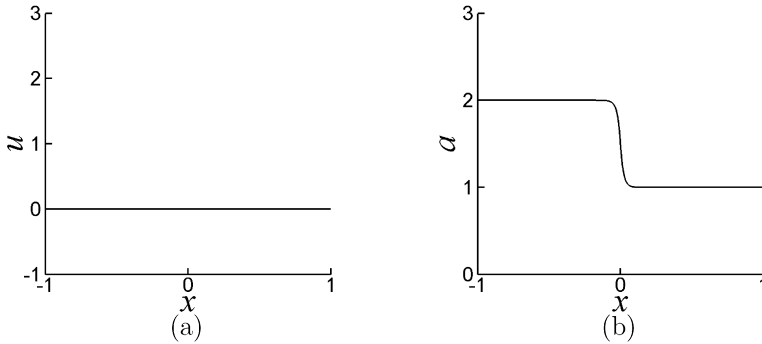
Fig. 3. The initial conditions for the perturbed Riemann problem. (a) The initial velocity profile is $u = 0$. (b) The initial speed of sound profile is a smoothed pressure jump.
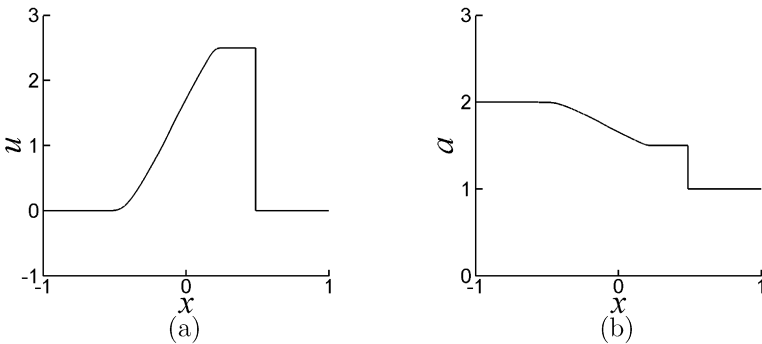

Fig. 4. The solution to the perturbed Riemann problem. The initial conditions are Eq. (56) that have been filtered with the Helmholtz filter. There is clearly a shock and an expansion wave. This is the solution at time $t = 0.2$.

6. Numerics

In Section 5.1.1 a numerical method is presented that will solve the Riemann problem. Here a numerical method is established that can be applied to more general initial conditions. In Section 7 we compare the behavior of the CAHE equations to the homentropic Euler equations. To accomplish this we use a numerical technique based on the characteristic structure of the CAHE equations. This technique is similar in nature to that used by Bhat and Fetecau [3]. Since the equations we are investigating are inspired by the use of averaged characteristics, our numerical method will track the characteristics as they evolve in time.

Our numerical method is interested in solving Eqs. (1) with initial conditions

$$v^+(x, 0) = v_0^+(x), \tag{57}$$

$$v^-(x, 0) = v_0^-(x). \tag{58}$$

Since we cannot operate on an infinite domain we restrict the problem to the domain $[a, b]$ and assume that on the boundaries

$$\frac{\partial}{\partial x} v^+(x, t) = 0, \tag{59}$$

$$\frac{\partial}{\partial x} v^-(x, t) = 0. \tag{60}$$

From Eqs. (25) and (27) we know that the value of $v^\pm$ does not change along its characteristics, thus

$$v^\pm\big(\phi^\pm(X)\big) = v_0^\pm(X) \tag{61}$$

where X is the label of the characteristic.

Let **x** be the equally spaced grid points on the interval $[-a, a]$. Let $\mathbf{X}^\pm$ be the positions of the characteristics X_i. These vectors can also be considered as the values of ϕ or as a dynamic grid. At time $t = 0$, $\mathbf{x} = \mathbf{X}^+ = \mathbf{X}^-$. Notationally let $v^\pm(\mathbf{x})$ be a vector containing the values of $v^\pm$ evaluated at points **x** and let $v^\pm(\mathbf{X}^\pm)$ be $v^\pm$ evaluated at the locations of the characteristics $\mathbf{X}^\pm$.

The positions of the characteristics are iterated in time, thus giving us the solution. A typical iteration proceeds as follows.

1. The values of $v^\pm(\mathbf{X}^\pm)$ are known and remain constant through time as a result of Eq. (61). The positions of the characteristics are known and thus the values can be interpolated onto the uniform grid, **x**, using cubic splines. This gives us the values $v^\pm(\mathbf{x})$.
2. From Eq. (16) we see that u and a are a linear combination of v^+ and v^-. Thus knowing the values of v^+ and v^- on the grid **x**, we can determine the values of u and a on the grid **x**. With these values the Helmholtz operator is then numerically inverted to give the values of $\bar{u}$ and $\bar{a}$ on **x** (details below). Cubic splines are again utilized to interpolate the values of $\bar{u} \pm \bar{a}$ on the characteristics, i.e. on the grids $\mathbf{X}^\pm$.
3. The positions of the characteristics, $\mathbf{X}^\pm$, are then iterated in time by the values of $\bar{u} \pm \bar{a}$ on $\mathbf{X}^\pm$ using the forward Euler's method.

In step 2, the Helmholtz operator is numerically inverted. To give a brief explanation of how the operator is inverted first consider a finite difference approximation of a second derivative on an equispaced grid:

$$\frac{\partial^2}{\partial x^2} f\big(x(i)\big) = \frac{1}{12\Delta x}\big[-1f(x_{i-2}) + 16f(x_{i-1}) - 30f(x_i) + 16f(x_{i+1}) - 1f(x_{i+2})\big]. \tag{62}$$

Thus the Helmholtz operator $(1 - \alpha^2 \frac{\partial^2}{\partial x^2})$ can be represented as a quintdiagonal matrix. This is easily inverted allowing the calculation of $\bar{u} \pm \bar{a}$ from $u \pm a$ on an equispaced grid.

A benefit to this method is that plotting the vectors $\mathbf{X}^\pm$ versus time gives a graph of the characteristic plane.

7. Comparisons with homentropic Euler equations

The CAHE equations were based on the homentropic Euler equations so naturally we compare the behavior of the two. In particular this section examines two examples chosen specifically to compare and contrast the equations behavior. Example 2 was chosen so that the CAHE equations would have a single traveling shock. The initial conditions for Example 2 are

$$u(x, 0) = \begin{cases} 5, & x < 0, \\ 0, & x \geqslant 0, \end{cases} \tag{63a}$$

$$a(x, 0) = \begin{cases} 2, & x < 0, \\ 1, & x \geqslant 0. \end{cases} \tag{63b}$$

Example 3 was chosen so that the homentropic Euler equations would have a single traveling shock. The initial conditions for Example 3 are

$$u(x, 0) = \begin{cases} 0, & x < 0, \\ -9.37440483\ldots, & x \geqslant 0, \end{cases} \tag{64a}$$

$$a(x, 0) = \begin{cases} 2, & x < 0, \\ 1, & x \geqslant 0. \end{cases} \tag{64b}$$

Examples 2a and 3a are the simulation of the homentropic Euler equations and 2b and 3b address the CAHE equations. In both examples the two sets of equations are found to behave significantly differently. This is attributed to the fact that the CAHE equations will not produce new characteristics as shown by the proof of Theorem 3.1, while the homentropic Euler equations do produce new characteristics.

7.1. Numerics for the homentropic Euler equations

Numerical simulations of the homentropic Euler equations require a separate method than that described in Section 6 because characteristics in the homentropic Euler equations collide and are created. For the numerical simulations of the homentropic Euler equations the Richtmyer method, a well-established if low order method, was utilized as described by [17]. This method is second order finite difference scheme and employs an artificial viscosity. Clearly this is not the most optimal numerical scheme for the Euler equations, but run at a sufficiently high resolution it will suit our purposes. For reference there were 2^{12} grid points on a $[-1, 1]$ domain. This method requires an artificial viscosity for stability when examining the Riemann problem. Several different values of ν were tested to see that the value did not significantly affect the solutions on the time interval examined. For the numerical simulations shown here, the artificial viscosity was set at $\nu = 0.08$.

7.2. Example 2

Example 2 (63) was chosen so that the CAHE equations would have a single traveling shock. Notice that with these initial conditions there is a discontinuity in the variable v^+, but v^- is constant. Since v^- is constant in the beginning it should remain constant for all time. This is a consequence of the fact that no characteristics are created or destroyed as time progresses.

7.2.1. Example 2b, the CAHE equations

Fig. 5 shows the simulation for Example 2b which examines the CAHE equations. The simulation was conducted with a resolution of 2^{12} and $\alpha = 0.02$. Figs. 5a and 5b show the single discontinuity progressing to the right as expected. Figs. 5c and 5d show the values of v^+ and v^-. The discontinuity in v^+ has traveled to the right and as expected v^- remains constant.

Figs. 5e and 5f show the paths of the v^+ and v^- characteristics respectively. Fig. 5e shows that the characteristics of v^+ are moving towards each other and as they near the shock are bent toward each other. They do not, however, intersect. Fig. 5f shows that the characteristics of v^- pass through the shock and upon doing so change their speed to match the characteristics on the other side.

7.2.2. Example 2a, the homentropic Euler equations

Now we examine the behavior of homentropic Euler equations for the same initial conditions. Fig. 6 shows the simulation for Example 2a. The simulation was conducted with a resolution of 2^{12}.

Figs. 6a and 6b show a shock progressing to the right as expected. In addition there is an expansion wave also occurring. Figs. 6c and 6d show the values of v^+ and v^-. Of primary notice is that v^- is no longer a constant but has attained new value. This is a significant departure from the behavior of the CAHE equations. Figs. 6e and 6f are not graphs of the actual simulation. The Richtmyer method does not lend itself to characteristic graphs as does the method used for the CAHE equations. Instead they are sketches that depict the behavior of the giving simulation.

The characteristics in v^+ change speed as they travel through the expansion wave. The characteristics intersect causing the shock. Thus at the shock the characteristics are destroyed.

For the v^- characteristics, at time $t = 0$, the characteristics to the left of the discontinuity have a speed greater than those to the right, but both are less than the speed of the shock. The result
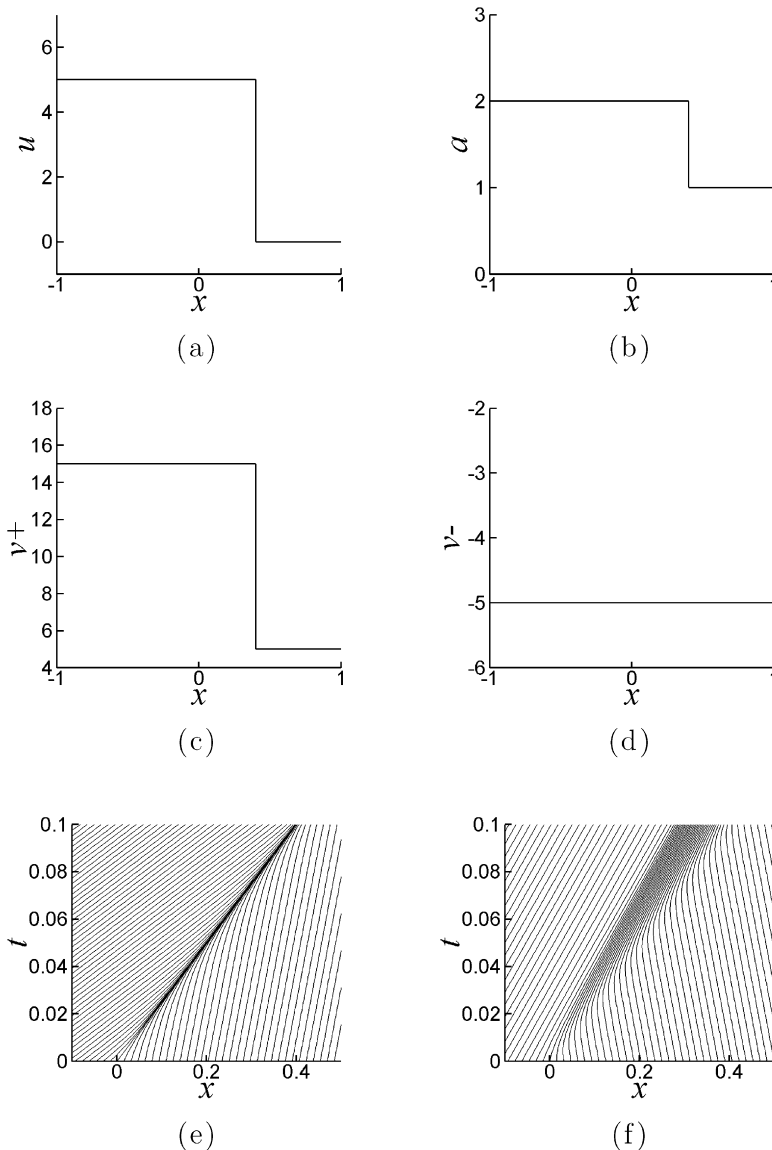
Fig. 5. Example 2b at time $t = 0.1$. This example was chosen so that the CAHE equations would have a single traveling shock which is clearly visible in the velocity and speed of sound in (a) and (b). (c) and (d) show graphs of the Riemann invariants v^+ and v^-. Note that v^- is constant as it was in the initial conditions. (e) and (f) show the v^+ and v^- characteristics respectively. Notice that the v^+ characteristics are converging to the shock but never intersect, while the v^- characteristics pass through the shock and change speeds as they do so.

is that the characteristics on the right will be absorb into the shock and between the characteristics on the left and the shock there will be a gap devoid of characteristics. This gap is filled with an expansion wave created at $t = 0$ and new characteristics that are created at the location of the shock continually as time progresses. The values of these new characteristics can be determined with the Rankine–Hugoniot jump conditions. This creation of characteristics again is a behavior that the CAHE equations does not demonstrate.
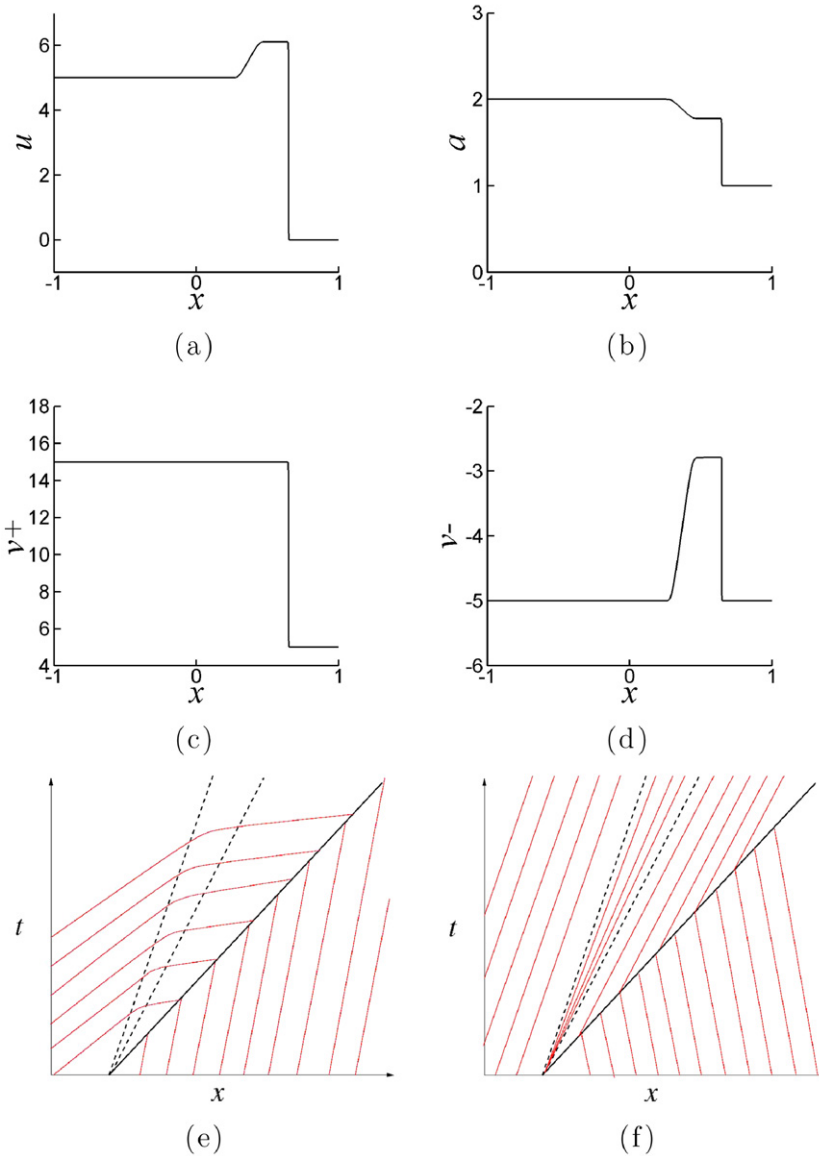
Fig. 6. Example 2a at time $t = 0.1$. While the CAHE equations form a single shock the homentropic Euler equations clearly form a shock and expansion wave. (a) and (b) show the shocks and expansion wave clearly in the velocity and speed of sound. (c) and (d) show the Riemann invariants v^+ and v^-. Notice that while v^- began as a constant it is no longer. This is due to the creation of new characteristics at the shock. (e) and (f) show sketches of the characteristics for this example. (e) shows that the v^+ characteristics are being absorbed by the shock. (f) shows the v^- characteristics being created at the shock. The dotted line represents the expansion wave.

7.3. Example 3

The previous example was chosen so that the CAHE equations would have a single shock. In contrast, Example 3 (64) was chosen so that the homentropic Euler equations would have a single traveling shock. Again a significant departure in behavior will be noticed.
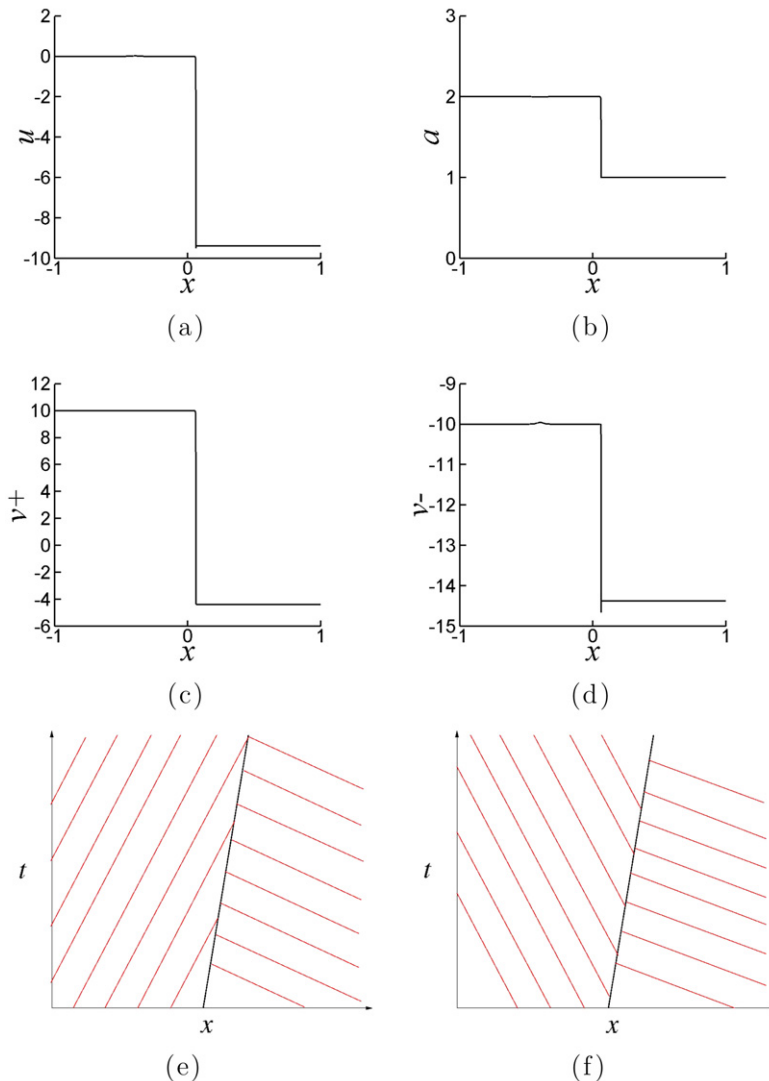
Fig. 7. Example 3a at time $t = 0.2$. This example was chosen to have a single shock for the homentropic Euler equations which is clearly visible in (a) and (b). The shock is moving to the right but clearly not as quickly as previous examples. (c) and (d) show the Riemann invariants v^+ and v^-. (e) and (f) are sketches of the characteristics for v^+ and v^-. Again in (f) v^- characteristics are being created at the shock.

7.3.1. Example 3a, the homentropic Euler equations

First we examine the behavior of homentropic Euler equations for Example 3a. Fig. 7 shows the simulation for Example 3a. The simulation was conducted with a resolution of 2^{12}.

Figs. 7a and 7b show a single shock. The shock is close to stationary but is progressing to the right. Figs. 7c and 7d show the values of v^+ and v^-. The discontinuity can be seen in both Riemann invariants. This is noticeably different than the behavior of the CAHE equations where a single traveling shock will appear in only one of the invariants.

As in the previous examples Figs. 7e and 7f are not graphs of the actual simulation, but sketches that depict the behavior of the giving simulation. The v^+ characteristics to the left of the discontinuity travel faster than those to the right with the speed of the shock found in between those speeds. Thus

the characteristics collide and cause the shock. The v^- characteristics to the left of the discontinuity travel faster than those to the right, however both are slower than the speed of the shock. Thus there is an area devoid of characteristics between the left characteristics and the shock. This is filled with new characteristics that originate from the shock.

7.3.2. Example 3b, the CAHE equations

Now we examine the CAHE equations for Example 3b. Notice that with these initial conditions there is a discontinuity in the both variables v^+ and v^-. Thus it is to be expected that there will be two phenomenon, either expansion waves or shocks. In this case, both will be shocks.

Fig. 8 shows the simulation for Example 3b. The simulation was conducted with a resolution of 2^{12} and $\alpha = 0.02$.

Figs. 8a and 8b clearly show two distinct shocks, close together, progressing to the left. These shocks can also be seen in Figs. 8c and 8d in the variables v^+ and v^-.

Figs. 8e and 8f show the paths of the v^+ and v^- characteristics respectively. The line across the center of the graph represents the remapping of characteristics as they had grown too close together for convenient computation. For both sets of characteristics there is a convergence of the characteristics towards the shock. This demonstrates that it is a stable discontinuity and that a perturbation will not turn these into expansion waves. Again the characteristics are bent towards each other, but never intersect.

7.4. Comparisons between the homentropic Euler and the CAHE equations

From these examples and previous sections we can begin to draw comparisons between the homentropic Euler equations and the CAHE equations.

Both sets of equations are capable of forming shocks and expansion waves from the Riemann problem. For homentropic Euler equations it is well established that for the Riemann problem there will often be both a shock and an expansion wave formed. With the CAHE equations, introduced in this paper, there will always be two shocks formed. However, if the initial conditions are slightly smoother, some of those discontinuities will be found to be unstable and result in an expansion wave. Thus both behaviors can be said to be found in both equations.

In terms of speed of the shocks, we have found there to be differences. In the homentropic Euler equations, the speeds of the shocks are determined by the Rankine–Hugoniot conditions, in order to preserve mass and momentum. With the CAHE equations the speed of a discontinuity is determined by the speed of the averaged characteristics at the location of the discontinuity. In Section 4, it can be seen that with the averaging chosen for this paper that the shock speed differs from those of the homentropic Euler equations. From this it is also clear that while the homentropic Euler equations may be formally regained from the CAHE equations by letting $\alpha \to 0$, the solution will not converge to weak solutions of the homentropic Euler equations. It may be possible, however, to choose an averaging scheme such that the shock speeds between the two equations are the same or similar.

Additionally the conditions under which a single traveling shock differs between the two equations as is demonstrated in Examples 2 and 3. For a single shock to form with the CAHE equations either v^+ or v^- must be constant. Even if it were possible to find an averaging scheme such that the shock speeds between the two equations are the same, these conditions would not change. For the homentropic Euler equations, the condition is tied in with the Rankine–Hugoniot conditions.

The final difference noted between these equations is significant. As seen in Examples 2 and 3, for the homentropic Euler equations, there can be areas devoid of characteristics. These can be filled with expansion waves or by new characteristics originating from the shock. By averaging the characteristics in the CAHE equations, there will be no areas devoid of characteristics. Thus there will be no generation of new characteristics. This can cause significant differences in behavior as seen in Example 2, where v^- remains a constant for the CAHE equations, but not for the homentropic Euler equations. This again is a property that is unaffected by the averaging scheme chosen.
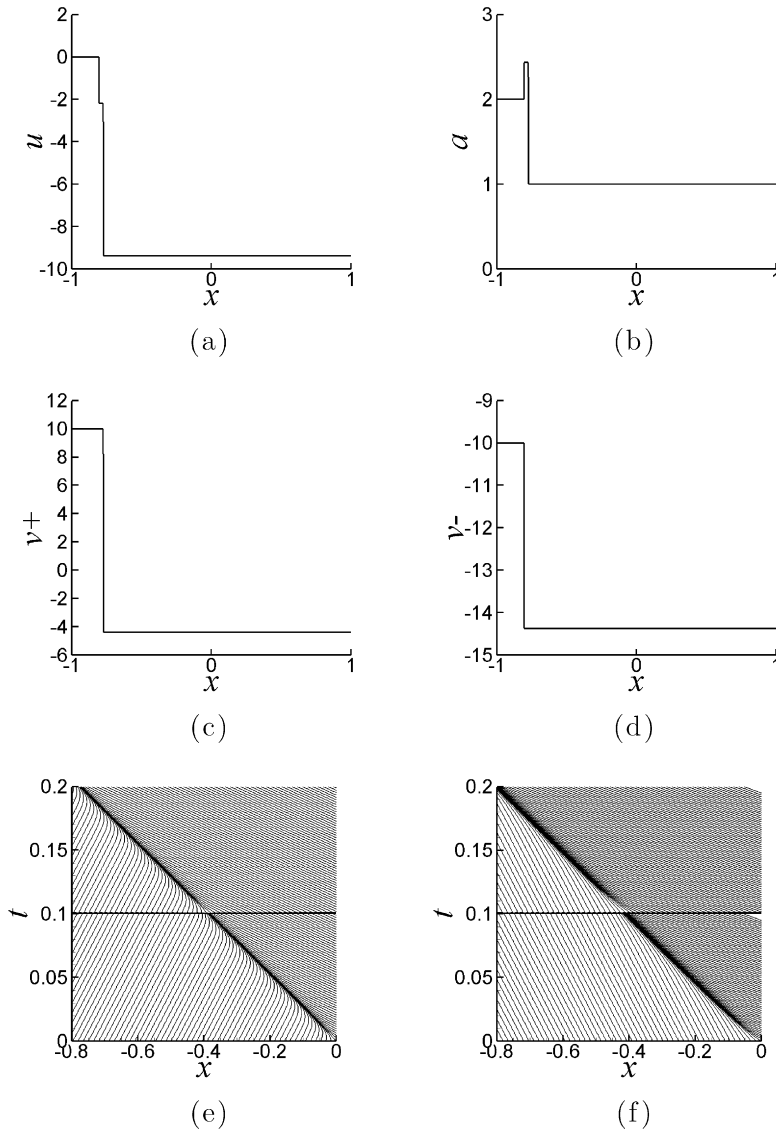
Fig. 8. Example 3b at time $t = 0.2$. (a) and (b) show that there are two distinct left traveling shocks in the velocity and speed of sound. (c) and (d) show that these shocks exist separately in the Riemann invariants v^+ and v^-. (e) and (f) show the characteristics for v^+ and v^-. The horizontal line at time $t = 0.1$ represents the remapping of the simulation. In both (e) and (f) the characteristics are converging to the shocks, while never intersecting.

8. Conclusions

The CAHE equations were derived by taking the homentropic Euler equations and spatially averaging the characteristics. This led to a new set of equations that has many interesting properties. Existence and uniqueness proofs, Theorems 3.1 and 3.2, were proven by establishing that the characteristics of the equations never intersect. In the process this established that any initial conditions in $C^1(\mathbb{R})$ will have a solution in $C^1(\mathbb{R})$. Furthermore any discontinuities in the initial conditions will remain and be convected in the solution for all time.

The speeds of shocks in the CAHE equations were found to be determined by the speed of the characteristics at the location of those shocks. Furthermore, different averaging schemes were shown to provide different shock speeds.

The Riemann problem was then examined, where solutions were generally found to consist of two traveling discontinuities. However, often one of the discontinuities can prove to be unstable and by smoothing the initial conditions will develop into an expansion wave instead.

Finally using some numerical examples and results from the previous sections the CAHE equations were compared and contrasted with the homentropic Euler equation from which they originated. Both can generate shocks and expansion waves from the Riemann problem. With the averaging scheme employed in the paper, the speeds of the shocks differ. For the examples chosen, the behavior of the equations proved to be significantly different. Finally, the homentropic Euler equations showed the generation of new characteristics, while with the CAHE equations, new characteristics will never be generated. From this it seems clear that as $\alpha \to 0$ the solutions to the CAHE equations will not converge to weak solutions of the homentropic Euler equations.

The CAHE equations have proven to have convenient existence and uniqueness properties. When continuous initial conditions are chosen, the solution will remain continuous. However, the equations seem to display behavior with too significant of departure from the homentropic Euler equations to be of use in gas dynamic applications. It is possible that this could be rectified by taken a one-sided average of the characteristics, but this concept was not pursued here.

References

[1] K. Mohseni, H. Zhao, J. Marsden, Shock regularization for the Burgers equation, AIAA paper 2006-1516, 44th AIAA Aerospace Sciences Meeting and Exhibit, Reno, NV, January 9–12, 2006.

[2] H.S. Bhat, R.C. Fetecau, A Hamiltonian regularization of the Burgers equation, J. Nonlinear Sci. 16 (6) (2006) 615–638.

[3] H.S. Bhat, R.C. Fetecau, Stability of fronts for a regularization of the Burgers equation, Quart. Appl. Math. 66 (2008) 473–496.

[4] G. Norgard, K. Mohseni, A regularization of the Burgers equation using a filtered convective velocity, J. Phys. A 41 (2008) 1–21.

[5] G. Norgard, K. Mohseni, On the convergence of convectively filtered Burgers equation to the entropy solution of inviscid Burgers equation, Multiscale Model. Simul. 7 (4) (2009) 1811–1837.

[6] D.D. Holm, M.F. Staley, Wave structures and nonlinear balances in a family of evolutionary PDEs, SIAM J. Appl. Dyn. Syst. 2 (2003) 323–380.

[7] A. Cheskidov, D.D. Holm, E. Olson, E.S. Titi, On a Leray-α model of turbulence, Proc. R. Soc. Lond. Ser. A Math. Phys. Eng. Sci. 461 (2055) (2004) 629–649.

[8] C. Foias, D.D. Holm, E.S. Titi, The Navier–Stokes-α model of fluid turbulence, Phys. D 152 (3) (2001) 505–519.

[9] J.E. Marsden, S. Shkoller, Global well-posedness of the LANS-α equations, Proc. R. Soc. Lond. 359 (2001) 1449–1468.

[10] K. Mohseni, B. Kosović, S. Shkoller, J.E. Marsden, Numerical simulations of the Lagrangian averaged Navier–Stokes (LANS-α) equations for homogeneous isotropic turbulence, Phys. Fluids 15 (2) (2003) 524–544.

[11] H. Zhao, K. Mohseni, A dynamic model for the Lagrangian averaged Navier–Stokes-α equations, Phys. Fluids 17 (7) (2005) 075106.

[12] D.D. Holm, J.E. Marsden, T.S. Ratiu, Euler–Poincaré models of ideal fluids with nonlinear dispersion, Phys. Rev. Lett. 349 (1998) 4173–4177.

[13] S.Y. Chen, C. Foias, D.D. Holm, E. Olson, E.S. Titi, S. Wynne, Camassa–Holm equations as a closure model for turbulent channel and pipe flow, Phys. Rev. Lett. 81 (1998) 5338–5341.

[14] H.S. Bhat, R.C. Fetecau, Lagrangian averaging for the 1D compressible Euler equations, Discrete Contin. Dyn. Syst. 6 (5) (2006) 979–1000.

[15] H.S. Bhat, R.C. Fetecau, J. Goodman, A Leray-type regularization for the isentropic Euler equations, Nonlinearity 20 (2007) 2035–2046.

[16] H.S. Bhat, R.C. Fetecau, J.E. Marsden, K. Mohseni, M. West, Lagrangian averaging for compressible fluids, Multiscale Model. Simul. 3 (4) (2005) 818–837.

[17] Culbert B. Laney, Computational Gasdynamics, Cambridge University Press, 1998.